Hybrid Auxetic Structures: Structural Optimization and Mechanical Characterization

Stefan Bronder, Marcel Adorna, Tomáš Fíla, Petr Koudelka, Jan Falta, Ondřej Jiroušek, and Anne Jung*

With their increased energy absorption capacity, auxetic materials are perfectly fit to develop new, enhanced lightweight crash absorbers for cars. Herein, the mass distribution along the struts is optimized via finite element analysis with a parameterized optimization. Four different auxetic unit cells are taken from the literature and their struts parameterize, the models simulate, and the mass specific energy absorption capacity optimizes. The two models with the highest energy absorption capacity are then selected for experimental investigation and produced by additive manufacturing from a polymer. To further enhance the mechanical properties, the specimens are electrochemically coated with nickel and the polymer molten out by pyrolysis. Those Ni/polymer hybrids are subjected to quasistatic and dynamic impact experiments. Only a small strain rate sensitivity can be detected under dynamic loading, namely, a higher plastic collapse and higher plateau stress. The hollow struts are folding instead of bending, which render them much weaker than predicted by the simulation. In conclusion, it is possible to improve existing crash absorber elements with tailored auxetic hybrid structures. They absorb higher amounts of energy without changing their stiffness under dynamic loading while saving mass and cost.

1. Introduction

The Poisson's ratio ν is defined as the negative ratio between the lateral strain and the longitudinal strain in loading direction.[1] Through the negative Poisson's ratio, auxetic structures have some special capabilities. From classical elasticity theory, lots of properties depend on the Poisson's ratio of the material.[2] The simplest example is the shear modulus G, with

$$G = \frac{E}{2(1 + \nu)} \qquad (1)$$

and the Young's modulus E. As the Poisson's ratio approaches its theoretical limit for an isotropic material of -1, the shear modulus goes to infinity. Other macroscopic effects of the negative Poisson's ratio are an increased thermal shock resistance,[3] a higher indentation resistance,[4–6] and a higher fracture toughness.[7,8] Due to that, auxetic structures offer higher energy dissipation[9,10] and a higher impact resistance,[4–6] which qualifies them as a suitable material for crash absorber elements in cars or as a core material for ballistic and blast protection.[11,12] Further applications of auxetic materials include press-fit fasteners, which take advantage of the contraction under compression to get the fastener inside. When trying to pull it out, the fastener resists by expanding due to its auxetic behavior.[13] Rivets can also be designed using the same mechanism. With the same concept, it would be possible to enhance biomedical components such as stands or arterial prostheses.[14]

However, the first artificially created material with a negative Poisson's ratio was a converted polyurethane (PU) foam manufactured in 1987 by Lakes.[5] He converted a conventional open-cell PU foam through triaxial compression and heating. This also marks the starting point for the investigation of tailored auxetic materials and as then many auxetic materials have been produced in the main material classes such as polymers, metals, ceramics, and composites.

Auxetic behavior in general is easiest explained in the 2D case. In 1985, Almgren[15] described the re-entrant honeycomb (**Figure 1**a) as a possible microstructure which displays that property.

Another geometry which exhibits auxetic behavior is based on the method of rotating squares[16] (e.g., Figure 1b). The squares are connected at the edges and can rotate freely. Under tension in one direction, this structure will expand in the perpendicular direction. It is also possible to connect rectangles, triangles, parallelograms, and so on, to get the same behavior. With these two mechanisms, the negative Poisson's ratio of many materials can be explained. For example in α-cristobalite, the rigid SiO_4 tetrahedrals are

S. Bronder, Prof. A. Jung
Applied Mechanics
Saarland University
Campus A4.2, 66123 Saarbrücken, Germany
E-mail: anne.jung@mx.uni-saarland.de

M. Adorna, Dr. T. Fíla, Dr. P. Koudelka, J. Falta, Prof. O. Jiroušek
Department of Mechanics and Materials
Czech Technical University
Na Florenci 25, 110 00 Prague 1, Czech Republic

(iD) The ORCID identification number(s) for the author(s) of this article can be found under https://doi.org/10.1002/adem.202001393.
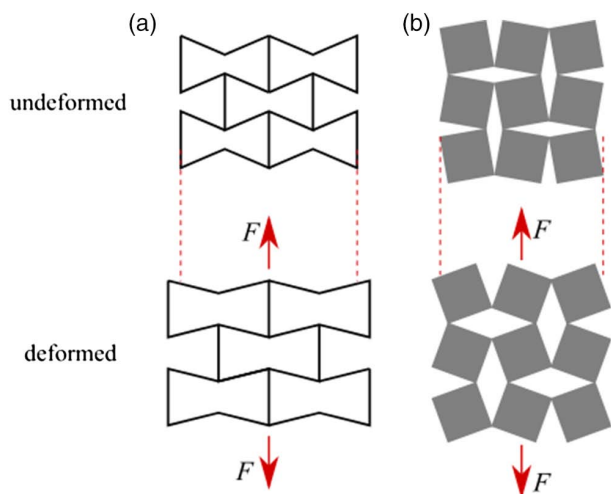
Figure 1. Two different mechanisms for negative Poisson's ratio: a) Re-entrant honeycomb as a 2D-structure and b) rotating squares as a 2D-structure. Both in undeformed state and under uniaxial tension.

connected at their edges and rotate freely.[17] Also 1/4 of all the cubic crystals display auxetic properties.[18] In recent years, other auxetic structures such as chiral lattices,[19] re-entrant hexagons,[20] or double arrowhead structures[21] have been proposed and investigated especially under dynamic loading conditions.[22–24]

Evans et al.[25] modified the structure of a polymeric molecule to display auxetic behavior through tailoring the chains into re-entrant honeycombs. However, this structure was too heavily cross-linked to be of practical use.[2] A more promising approach was proposed by He et al.,[26] in 1998. They suggested a liquid crystalline polymer (LCP) with rigid rod molecules connected by flexible spacer groups along the chain. The spacer groups are either attached to the sides of the rigid molecules or to their ends. In a relaxed state, the rod molecules are oriented along the chain, when stretched the rods with the connection on their sides rotate and thereby cause an increase in the interchain separation.

Another interesting field for auxetic materials is fiber-reinforced composites. An approach to achieve auxetic behavior in such a composite is to choose a suitable stacking sequence of the fiber layers.[27,28] In addition, the individual lamina material is required to be highly anisotropic, which makes carbon fiber/epoxy resin a more suitable choice compared with Kevlar/epoxy resin or glassy fiber/epoxy resin.[2] Due to the resulting auxetic behavior, the composite shows increased resistance to low velocity impacts and static indentation.[29] The auxetic composites furthermore display a more localized initial damage and therefore no large delaminations, which means that less of the material needs to be repaired.[2] A different approach is to use auxetic fibers within the composite,[30] which would resist fiber pull-out. The mechanics are the same as for an auxetic fastener.[13]

Through a combination of finite element analysis (FEA) and additive manufacturing (AM) methods, it is possible to manufacture auxetic cell-structures tailored for a certain application.[31] For topology optimization in FEA, usually a bidirectional evolutionary structural optimization (BESO) method[32] or solid isotropic microstructures with penalization (SIMP) method[33] is used. However, to save time and computational resources, the optimization in this work was carried out using existing auxetic unit cells and introducing geometry parameters to them. For the optimization of the geometry parameters, a variation of the Broyden–Fletcher–Goldfarb–Shanno (BFGS) algorithm[34–37] was used, which is one of the many quasi-Newton procedures available.[38] An advantage of the quasi-Newton procedures is that they only need the first derivative and approximate the Hessian matrix, which saves computational time.[38] Also Newton and quasi-Newton methods converge much faster to a solution than steepest descent for example. The BFGS algorithm furthermore has effective self-correcting properties in the approximation of the Hessian, which prevents the iterations from slowing down. Byrd et al.[39] further developed the BFGS routine to include the possibility of a global constraint or the limitation on parameters. This limited BFGS for Bound Constrained (L-BFGS-B) algorithm also saves computational capacity and reduces computational time.

An AM method for polymers is defined as a material connection procedure where the 3D object is created layer-wise.[40] The basic routine for all AM procedures is the same. At first, there exists a meshed 3D computer model either reconstructed from images or created with a computer-aided design software. From that, a surface tessellation language (STL) file will be created through approximation of the surface with triangles. This STL file then gets sliced into 2D layers, which will be produced by an AM device.[41] There are many different polymers available for AM, i.e., acrylonitrile butadiene styrene (ABS),[42] polylactic acid (PLA),[42] polyamide (PA),[43] or epoxy resins.[44] Because of the diversity of materials, AM methods have a great potential for applications in aerospace industry, complex lightweight structures, architectural models, art or bioprinted organs.[41] But there is still a lack of stiffness and functionality, which prevents a wide industrial usage of AM.[41]

All specimens in this contribution were produced using a 3D polyjet procedure. The polyjet is similar to an inkjet printer. The print head moves in x- and y-directions while applying thin photopolymer layers.[45] After finishing one layer, it gets hardened using ultraviolet (UV) light, which substitutes the hardening process of other AM methods.[46] The highest layer-resolution is 16 μm, which is high in comparison with, i.e., selective laser sintering (SLS). But the parts manufactured with polyjet printing are weak compared with other manufacturing procedures.[47] As single materials have a limit to their capabilities, a further improvement is possible through combining materials and thus combining their strengths. This combination leads to the fabrication of a hybrid material.

The aim of this work is to use FEA to optimize different auxetic cells to achieve a higher energy absorption capacity for crash elements. The structures with the highest energy absorption capacity are 3D polyjet printed and reinforced with a coating of nanocrystalline nickel. Those hybrid structures are cheaper in production than a directly additively manufactured nickel specimen. In addition, there is a much higher structural resolution possible with polyjet printing. The specimens are then investigated under quasistatic compression and during the dynamic impact by Open Hopkinson Pressure Bar (OHPB).

2. Experimental Section

The main goal of this contribution was to optimize an existing auxetic unit cell with respect to its energy absorption capacity. Therefore, a geometry optimization via FEA of a quasistatic loading scenario was carried out first. Then quasistatic compression experiments were conducted to verify the simulation results. The specimens were further improved with a nickel coating to enhance the additively manufactured polymer structure. Those specimens were also studied in quasistatic experiments to quantify the improvement. Finally, all specimens were subjected to dynamic experiments to validate the suitability of the structure for crash absorbers.

2.1. Modeling and Structural Optimization

The simulation and optimization was divided into two different steps and two different self-programmed Python scripts. This split construct was chosen because the commercial FEA tool ABAQUS does not include all necessary Python packages.

Therefore, one script handled the optimization, whereas the other one is controlling the ABAQUS simulation.

The used auxetic unit cells were taken from the literature[48–50] and are shown in **Figure 2**. The different unit cells will further be referred to as structure-1 (S-1), structure-2 (S-2), structure-3 (S-3), and structure-4 (S-4). The unit cells S-1, S-3, and S-4 were based on the principle of the re-entrant honeycomb, whereas S-2 was based on the method of missing ribs. Every unit cell was introduced with the geometry parameters waist (x) and strut thickness (y) (Figure 2), which were to be optimized.

2.1.1. Optimization Routine

The main Python script automated and controlled the optimization. It managed the database of geometry parameters and their association to the energy absorption capacity, as well as the minimizing of the objective function. The objective function was a surrogate model and (Equation (2)) linked the geometry parameters to the energy absorption capacity. It was chosen as a simple multidimensional quadratic polynomial. In the form of
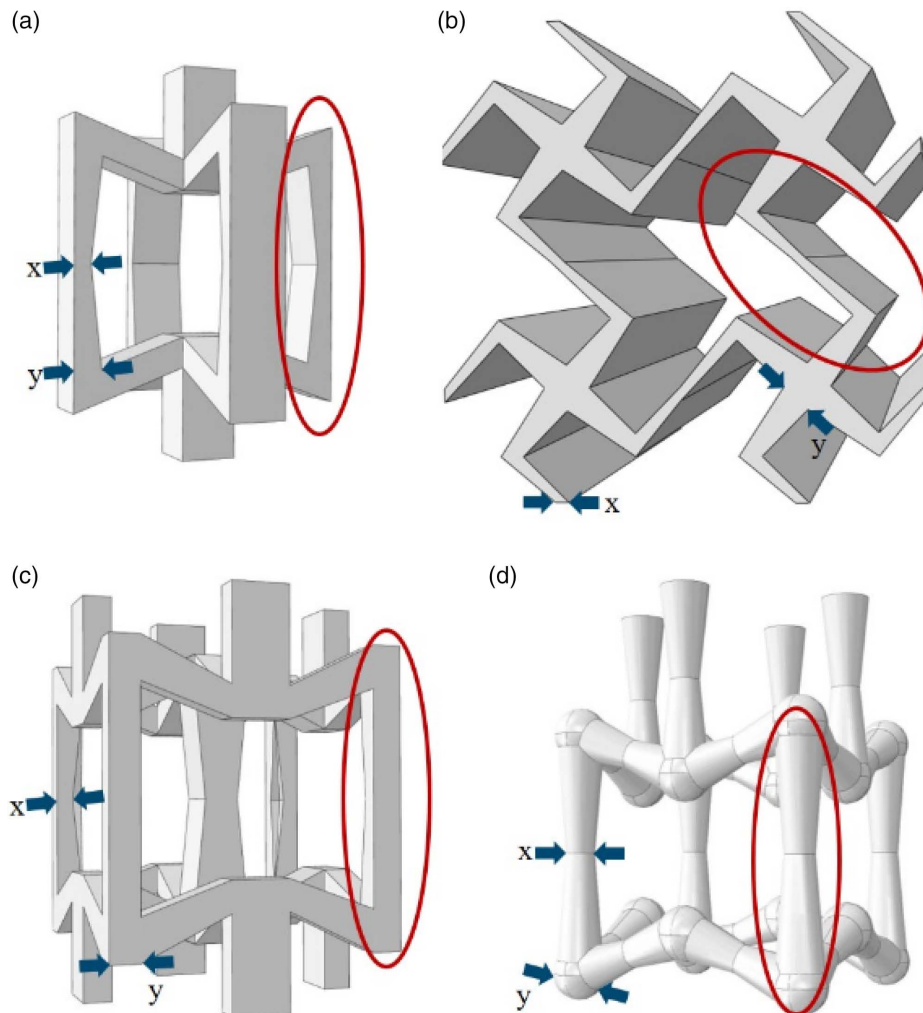

Figure 2. Four 3D auxetic unit cells (S-1 to S-4) with geometry parameters waist (x) and strut thickness (y), marked in red is a representative strut; a) S-1, b) S-2, c) S-3, and d) S-4. These unit cells were optimized to maximize the energy absorption capacity with respect to the geometry parameters.

**ADVANCED
SCIENCE NEWS**

www.advancedsciencenews.com

**ADVANCED
ENGINEERING
MATERIALS**

www.aem-journal.com

$$A = ax + bx^2 + c\gamma + c\gamma^2 + ex\gamma + f \qquad (2)$$

only six known points were required to find a fit-function, which reduced the number of simulations in the beginning. A denotes to the mass-specific energy absorption capacity, a, b, c, d, e, and f are curve parameters and x and y are the two geometry parameters defined for each structure. There also existed a global minimum as the function was quadratic, as a further advantage of this simple surrogate model. This optimization method corresponded to a response surface technique. Through finding the minimum, the energy absorption capacity is maximized while reducing the overall mass of the structure.

After six simulations with random geometry parameter pairs, the first fitting of the objective function by the method of the least squares can be done, which determined the curve parameters a, b, c, d, e, and f. Afterward, the minimum of that function was determined by the L-BFGS-B algorithm to find a new set of geometry parameters. The geometry parameters were constrained to physically sensible values and thereby guaranteeing a convergence of the minimizer either at a minimum or at the edges of the geometry space. A new simulation was carried out with these new parameters and the resulting energy absorption capacity as well as the mass of the model was added to the database. The objective function was then fitted to the extend database, a new minimum was determined and a new simulation was carried out. The update of the objective was due to a possible change in the curve parameters and thereby a change in the minimum, as the objective function was more reliable with more simulations. This loop was repeated until the difference between the mass-specific energy absorption capacity of the last iteration and the mass specific energy absorption capacity of this iteration is less than 0.1%.

2.1.2. Simulation Routine

The subprocess handled the FEA via ABAQUS and the data extraction from the ABAQUS result file. First of all, the geometry parameters were read and two auxiliary parameters for the model construction were calculated. This was followed by the construction of the structure, the material model, the meshing, and the assembly of the respective parameter set with the ABAQUS specific libraries for Python. The unit cell was constructed for the structural design (dimensions $W \times D \times H = 10 \times 10 \times 14 \, mm^3$) and tripled in every spatial direction to build the macroscopic assembly. The only exception is the elementary cell of S-2 (dimensions $W \times D \times H = 10 \times 30 \times 10.5 \, mm^3$), which was only tripled in length direction and quadrupled in height direction. The overall assembly of the structures thus had a volume of approximately $37.8 \, cm^3$.

A dynamic-explicit model was used to simulate the compression test, as the deformations were too big to use an implicit model. The auxetic structure was perceived as a 3D-deformable object, which was placed between two discrete rigid plates (**Figure 3**) and was compressed to 2/3 of its length. The compression was sufficient for comparability, as the plateau phase in the stress–strain diagram was reached, which was assumed to be constant. The densification area at the end of compression was not relevant for energy absorption and was therefore not considered.
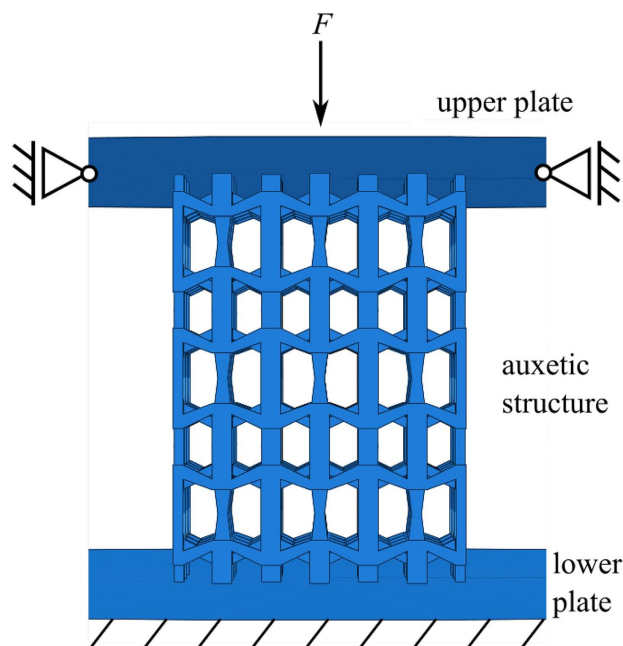

Figure 3. Exemplary simulation assembly of the structure S-3 for the compression experiment including boundary conditions. The specimen of $3 \times 3 \times 3$ unit cells is compressed between two rigid plates. The lower plate is fixed, whereas the upper plate moves down.

Table 1. Quasistatic material data of the polyjet printed polymer EX200.

Density [$g \, cm^{-3}$]	1.02
Young's modulus [MPa]	1283
Tensile Strength [MPa]	42.4
Elongation at break [%]	6.83

An elastic plastic material model on the basis of the printer polymer VisiJet EX200 plastic (**Table 1**) was used for the simulation. The Poisson's ratio of the printer material was assumed to be 0.33.

The deformation in the simulation was realized via the boundary conditions of fixing the lower plate, whereas the upper plate moved 14 mm down. A friction penalty with a friction coefficient of 0.1 was applied to the contacting surfaces of plate and structure to mimic the real experimental setup. The contact was modeled with Coulomb friction. The deformation was applied within 2.5 s, thus only low kinetic energies were generated. The plates and the auxetic structure were meshed using quadrilateral-elements (R3D4) and tetrahedral-elements (C3D10M), respectively.

After finishing the calculation, the reaction force and displacement values of the upper plate from the result database (ODB) were used for further calculations. A mean of all force values F was calculated and multiplied with the total displacement u of 14 mm to calculate the energy absorption capacity E_{total} of the structure (Equation (3)).
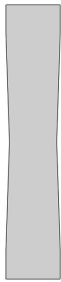
$$E_{total} = u \cdot \frac{\sum\limits_{n} F_n}{n} \qquad (3)$$

where n is the number of force values. This method corresponded to a numerical integration in which the area under the curve was approximated as a rectangle. The model's mass was calculated from the model-database (MDB) and was passed back to the main script together with the energy absorption capacity.

2.2. Specimens—Manufacturing and Coating

The two models with the highest energy absorption capacity were selected for the experimental analysis. The specimens were manufactured using the 3D polyjet printer Pro Jet HD3000 (3D Systems, Rock Hill, USA) from VisiJet EX200 plastic with the highest resolution ($656 \times 656 \times 800$ DPI). Thus, a single polymer layer was $29\,\mu m$ thick. To fit the specimens into the OHPB testing device, the model from the simulation was scaled by a factor of 0.42, so the overall specimen dimensions of S-3 were $\approx 12.5 \times 12.5 \times 18.4\,mm^3$ and of S-4 $\approx 13.7 \times 13.7 \times 19.5\,mm^3$.

Table 2. Strut forms and parameters for the three differently produced specimen types.

Structure	S-3	S-4A	S-4B
Strut			
Strut thickness [mm]	0.84	0.84	0.84
Waist [mm]	0.73	0.37	1.10

For verification of the optimization, an additional specimen type of S-4 with different geometry parameters was produced. Hence, the optimized version of S-4 will further be referred to as S-4B, the other version will be referred to as S-4A. **Table 2** shows an overview of the different specimen types.

To reinforce the polymer specimens and thus create a hybrid material, an electrochemical coating of 60 and $120\,\mu m$ nickel was applied. Therefore, a deposition cell consisting of the specimen as cathode, an anodic cage with the sacrificial anode, and an electrolyte was necessary. To be able to electrochemically coat the polymer specimens, they must first be made electrically conductive. This was achieved with a thin layer of graphite lacquer, which was applied by dip coating in the liquid lacquer.[51] The specimen was then connected with copper wires and positioned centrally within the anodic cage. The anodic cage consists of a double-walled hollow cube with polyvinylidene difluoride edges and titanium expanded metal side walls. Small nickel pellets were filled into the side walls as sacrificial anode. As the side walls were electrically insulated from each other, each side wall must be connected to the anode of the galvanostat by means of a six-legged spider conductor.

The specimen was connected to the cathode of the galvanostatic power supply and the anodic cage was put into the electrolyte until it was completely immersed. A commercial nickel sulfamate electrolyte ($110\,gL^{-1}$ Ni, Enthone GmbH, Langenfeld, Germany) was used, which was heated to keep a constant temperature of $20\,°C$. All specimens were coated with a mean current density of $1.5\,mA\,cm^{-2}$.

The surface area of the structures was calculated from the ABAQUS model. For more details on the deposition process, the reader is referred to previous works.[51–54] To increase ductility and reduce further weight the coated specimens were heated in an oven at a temperature of $300\,°C$, and the polymer was molten out. These specimens will further be referred to as hollow strut structures.
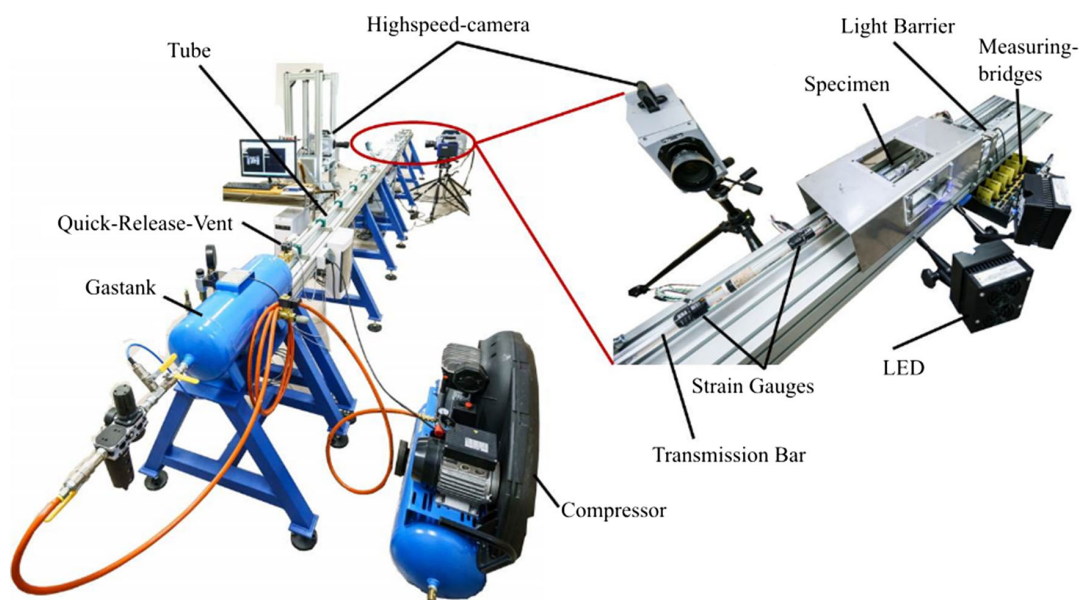

Figure 4. OHPB setup with the main components. A zoom in of the specimen chamber is on the right side.

**ADVANCED
SCIENCE NEWS**

www.advancedsciencenews.com

**ADVANCED
ENGINEERING
MATERIALS**

www.aem-journal.com

2.3. Quasistatic Experiments

The quasi-static compression experiments were carried out with a strain rate of $3e - 3s^{-1}$ utilizing the universal testing machine EletroPlus E10000 (Ltd. Instron, Pfungstand, Germany) and the custom-made microtensile test[55] at the chair of Applied Mechanics at Saarland University. All experiments were observed with a 9 mega-pixels CCD (charge-coupled device) camera (Manta G-917B, Allied Visions Technologies GmbH, Puchheim, Germany) to evaluate the local deformation with digital image correlation (DIC). The frame rate was coupled with the movement of the machine so every 0.25% strain one picture was taken. The DIC was carried out using the commercial software Istra 4D (Dantec Dynamics, Skovlunde, Denmark). For the purpose of a DIC analysis, the specimens were primed white and a fine irregular speckle pattern was sprayed on the specimens with an airbrush pistol. All quasistatic experiments were conducted on pure polymer, Ni/polymer hybrid and hollow strut specimens.

2.4. Dynamic Experiments

The dynamic experiments were conducted using the OHPB setup[56] of the Department of Mechanics and Materials at Czech Technical University (CTU) in Prague (**Figure 4**). The OHPB setup was chosen to achieve a larger overall deformation and its better suitability for cellular materials compared with the Split Hopkinson Pressure Bar (SHPB) test.[56] Typical car crash velocities are in the range of 45–90 km h^{-1}, thus the strain rates 400 and 800 s^{-1} were investigated as they are in the range of these impact velocities.

In the OHPB configuration, the specimen was attached to a long bar. A second bar of the same length was accelerated with a gas gun and directly impacted the specimen. In the following text, the bar with the specimen was referred to as the transmission bar and the accelerated bar as the impact bar. Both bars were made of polymethyl methacrylate (PMMA) and were 1.6 m long. PMMA bars were used due to the low plateau forces of the pure polymer specimens. The lower mechanical impedance corresponding better to the specimens in comparison with metal bars and results in a lower signal-to-noise ratio. This led to a better force resolution. For signal measurement, 12 individual strain gauges were attached to the bars and interconnected to form wheatstone half bridges. Four of them were attached to the impact bar at a distance of 200 mm from the impact surface. The remaining ones were attached in groups of four to the transmission bar at a distance of 200 and 400 mm from the specimen. At each measuring point, two foil strain gauges (1-LY61 3/120, HBM, Germany) and two semiconductor strain gauges (AFP 500-090, Kulite, USA) were glued on and connected to a total of six half bridges. The experiments were all recorded with a high-speed camera (Fastcam SA-Z 2100 K-M-32 GB, Photron, San Diego, USA). The specimen was illuminated by light-emitting diode (LED) light sources (Multiled QT, GS Vitec, Germany). The specimens for DIC were all provided with a speckle pattern on one side (varnish: Dupli Color, Effect: Granite). To measure the impact speed, two light barriers were installed just in front of the specimen.

All specimens were embedded in acrylic resin on one side to allow parallel grinding of the surfaces (embedding material:

VariKleer, Buehler, Esslingen am Neckar, Germany). A frequency-related viscoelastic model of the bars was used to calculate the stress and strain from the strain gauge signal and the bar dimensions. Further information on the calculation of the signal can be found in the literature.[56,57]

3. Results

3.1. Simulation

After the optimization, S-3 and S-4 displayed the highest energy absorption capacity (**Figure 5**), which made them the chosen
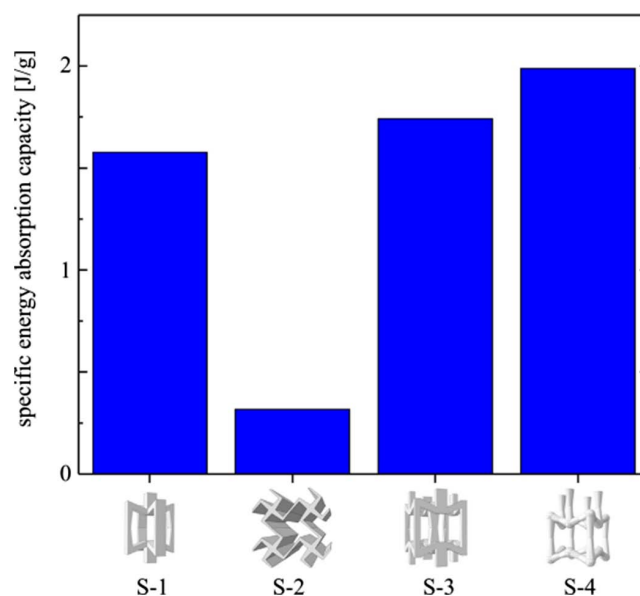

Figure 5. Comparison between the maximized energy absorption capacities of the four structures resulting from the simulated compression tests.
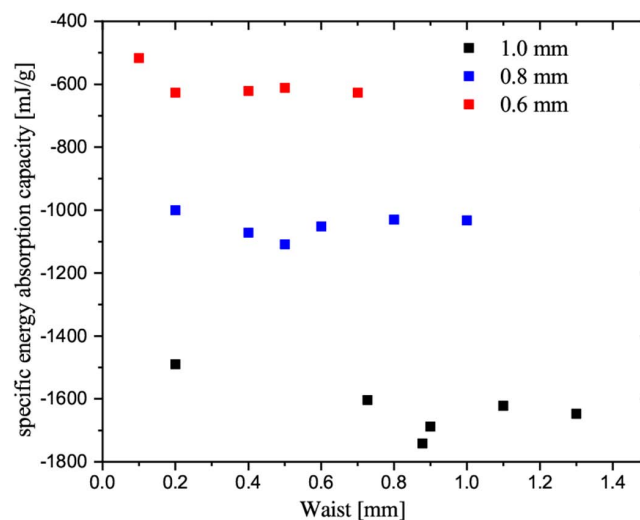

Figure 6. Energy absorption capacity calculated from simulation versus waist dimension for three different strut thicknesses of S-3. The amount of absorbed energy is strongly increasing with increasing strut thickness.

**ADVANCED
SCIENCE NEWS**

www.advancedsciencenews.com

**ADVANCED
ENGINEERING
MATERIALS**

www.aem-journal.com

structures for specimen production by AM and coating as well as for experimental investigation. Both structures were based on the re-entrant honeycomb principle. S-2 exhibits a much lower energy absorption capacity due to its two-dimensionality and hence a much higher mass.

For S-3, the specific energy absorption capacity increases strongly with increasing strut thickness. In contrast, the waist exhibits a weaker influence on the energy absorption capacity (**Figure 6**). The negative sign of the specific energy absorption capacity results from the negative sign of the force calculated by the finite element method (FEM) simulation. The edgy structure and the sharp waistline associated with it act like a notch and
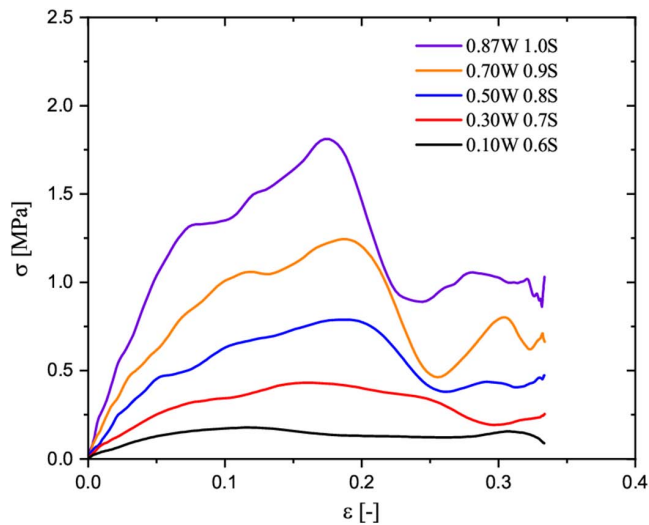
thus weaken the struts. In addition, the waist does not reduce the mass significantly for this structure.

Different optimum waist values exist for different strut thicknesses, but there is a nonlinear correlation. The plastic collapse stress (PCS) as well as the plateau stress increase significantly toward the optimized geometry parameters, which are 0.87 mm for the waist and 1.0 mm for the strut thickness (**Figure 7**). PCS refers to the peak stress after the pseudoelastic regime, which is the linear part at the beginning of the stress–strain diagram.

Figure 7. Stress–strain diagrams of S-3 for different strut thicknesses (S) with different waist thicknesses (W); the graphs have been smoothed by the LOWESS algorithm for better illustration. The optimized version of S-3 has a waist of 0.87 mm and a strut thickness of 1 mm.
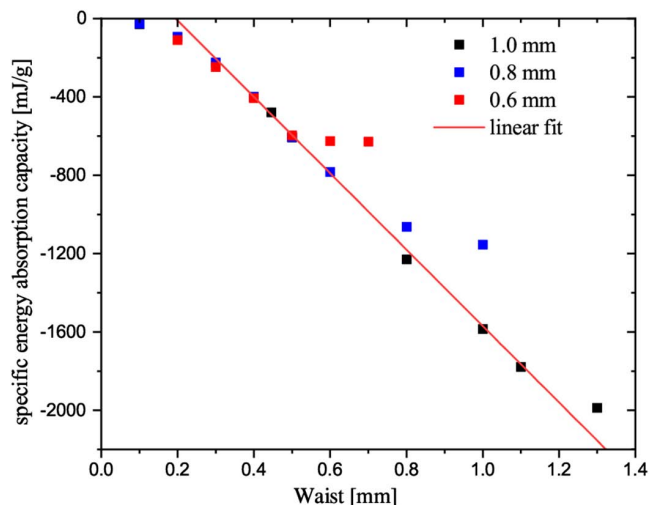

Figure 8. Energy absorption capacity calculated from the simulation versus waist dimension for different strut thicknesses of S-4 and a linear fit. This linear fit approximates the energy absorption capacity for S-4 with tapered or circular struts.
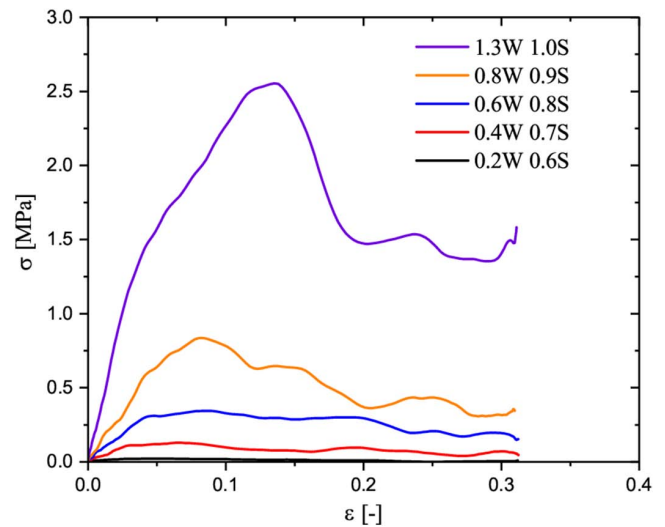

Figure 9. Stress–strain diagrams of S-4 for different strut thicknesses (S) with different waist thicknesses (W); the graphs have been smoothed by the LOWESS algorithm for better illustration. The optimized version of S-4 has a belly of 1.3 mm and a strut thickness of 1 mm.
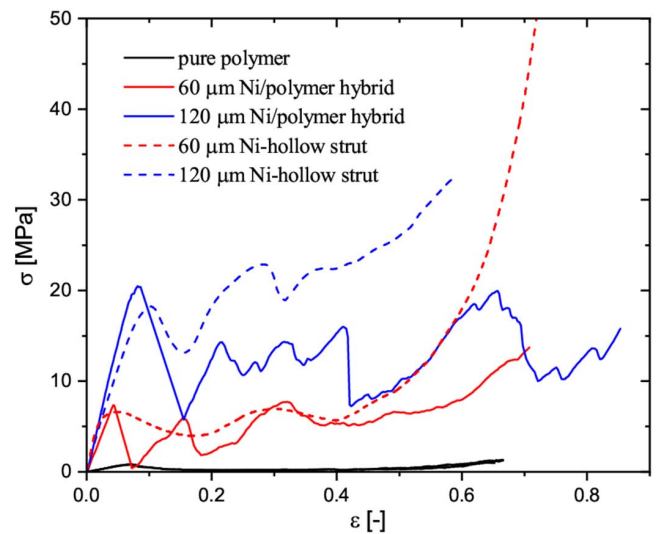

Figure 10. Average stress–strain diagrams for the pure polymer, Ni/polymer hybrid structures and Ni-hollow strut structures of S-3. The nickel coating improves the PCS and plateau stress. The hybrid specimens fail brittle, whereas the hollow strut specimens are more ductile. About 120 μm of nickel coating does more than double the PCS and plateau stress compared with the 60 μm.

The plateau stress identifies the nearly constant stress following the PCS peak. A mean value over the stresses in the plateau phase is calculated as the plateau stress. The simulations were only carried out up to 33% compression for the sake of time efficiency, as the plateau area was assumed to be approximately constant.

Table 3. Mean energy absorption capacity per mass per volume ($E/(m \times V)$) for the pure polymer specimens (0 µm), the Ni/polymer hybrid specimens (hybrid) and the hollow strut specimens (hollow strut) for both nickel coating thicknesses. No hybrid specimens of S-4B were manufactured due to the brittle failure of the hybrid specimens observed with S-3 and S-4a. The hollow strut specimens increase the energy absorption capacity compared with the hybrid specimens. Due to a small plateau stress, the energy absorption capacity of S-3 is slightly higher than for S-4B.

$E/(m \cdot V)$ [J g^{-1} mm^{-3}]	S-3		S-4A		S-4B	
	Hybrid	Hollow strut	Hybrid	Hollow strut	Hybrid	Hollow strut
0 µm	0.145	–	0.0164	–	0.097	–
60 µm	0.498	0.564	0.146	0.300	–	0.208
120 µm	0.721	1.132	0.178	0.667	–	0.404

In the case of S-4 (**Figure 8**), the waist has a stronger influence on the energy absorption capacity compared with S-3. The strut thickness lowers the attainable minimum, but there are no jumps between the strut thicknesses as seen for S-3. The linear part in Figure 8 outlines a strong coupling between waist and strut thickness for this structure. Through a linear fit with

$$A = -1950 \, \text{mJ g}^{-1} \, \text{mm}^{-1} w + 380 \, \text{mJ g}^{-1} \qquad (4)$$

for the waist w, it is possible to estimate the specific energy absorption capacity A for circular struts. The optimized version of S-4 has a belly instead of a waist, hence the struts are the weak points for this structure. The belly resists a buckling of the struts.

The optimization increases the PCS and the plateau stress approaching the optimized version with a waist of 1.3 mm and a strut thickness of 1.0 mm (**Figure 9**).

3.2. Quasistatic Compression Experiment

The auxetic Ni/polymer hybrid specimens show brittle failure, which significantly reduces the energy absorption capacity. In contrast, the hollow strut structures are more ductile and thus are able to absorb higher amounts of energy (**Figure 10**). The heating in the oven does not reduce the stiffness or the PCS compared with the hybrid structures. The nickel coating increases
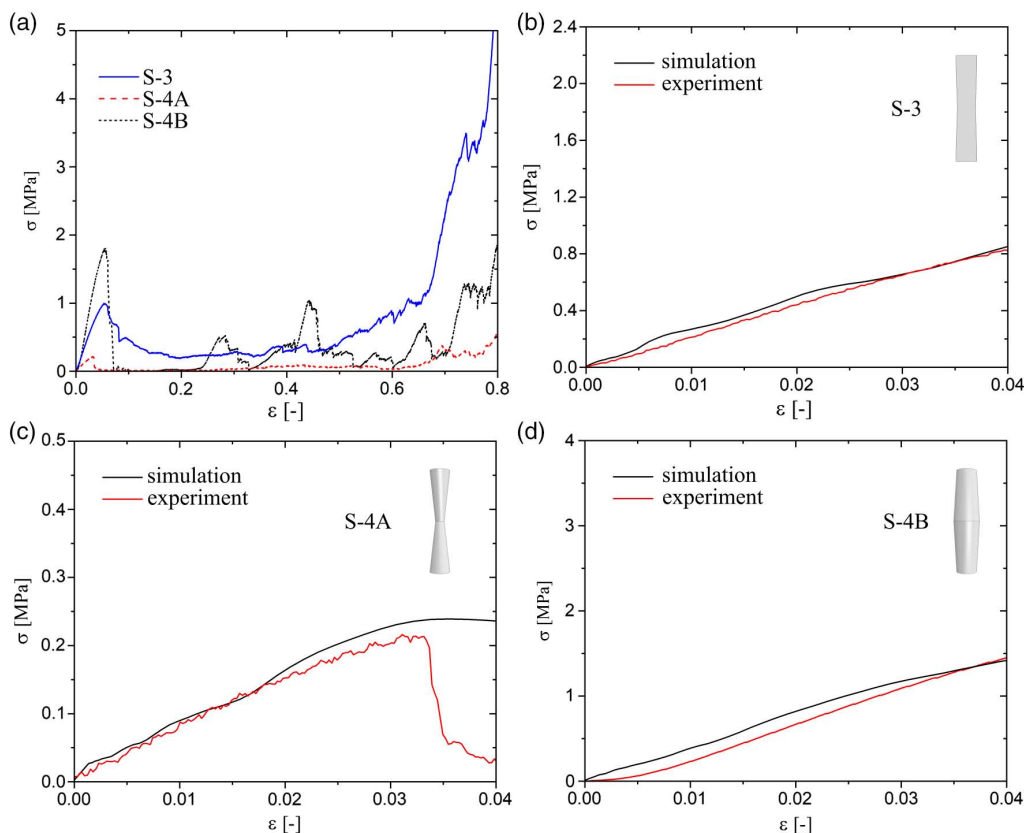

Figure 11. Average stress–strain diagrams comparing a) the pure polymer compression tests of each structure, b) simulation and compression test of S-3, c) simulation and compression test of S-4 A, d) simulation and compression test of S-4B. The polymeric specimens display brittle failure. The simulations match the experiment within the elastic part up to ≈4% strain. The optimized S-4B specimens display the highest stiffness and highest PCS, which is in accordance with the optimization results.

stiffness, PCS, and plateau stress significantly compared with the uncoated polymer specimens. The overall mean energy absorption capacity normalized by volume and by mass for all specimens is shown in **Table 3**. The volume normalization is due to different sizes of the specimens, whereas the mass normalization is to account for the lightweight factor in the optimization. All values and diagrams are the mean of three experiments.

The comparison of all uncoated specimens (**Figure 11**a)) verifies the optimization results, that S-4B is the structure with the highest PCS. But as the polymer fails brittle, there is only a negligible plateau stress. This leads to a lower energy absorption capacity than for the specimens of S-3 (Table 3).

The simulation results are well matched by the experiments in the elastic region up to ≈5% strain (Figure 11b–d)). But as

the model did not contain failure, the simulation shows a plateau which does not exist in the experiments due to the brittle failure. In addition, the printed polymer displayed a lower plastic strain than the material data provided by the manufacturer predicted.

Another reason for the difference between the simulation and the experiments is the different local deformation mechanism in the experiments with the pure polymer specimen, which is outlined by the DIC analysis (**Figure 12**). As the struts of the manufactured specimens are fixed on the upper and lower plates, they cannot move freely. The simulation also predicted a folding of the cell layer. In the experiment, the specimen began to shear off in one direction (Figure 12 $\varepsilon = 11\%$). However, these discrepancies between experiment and simulation have no impact on
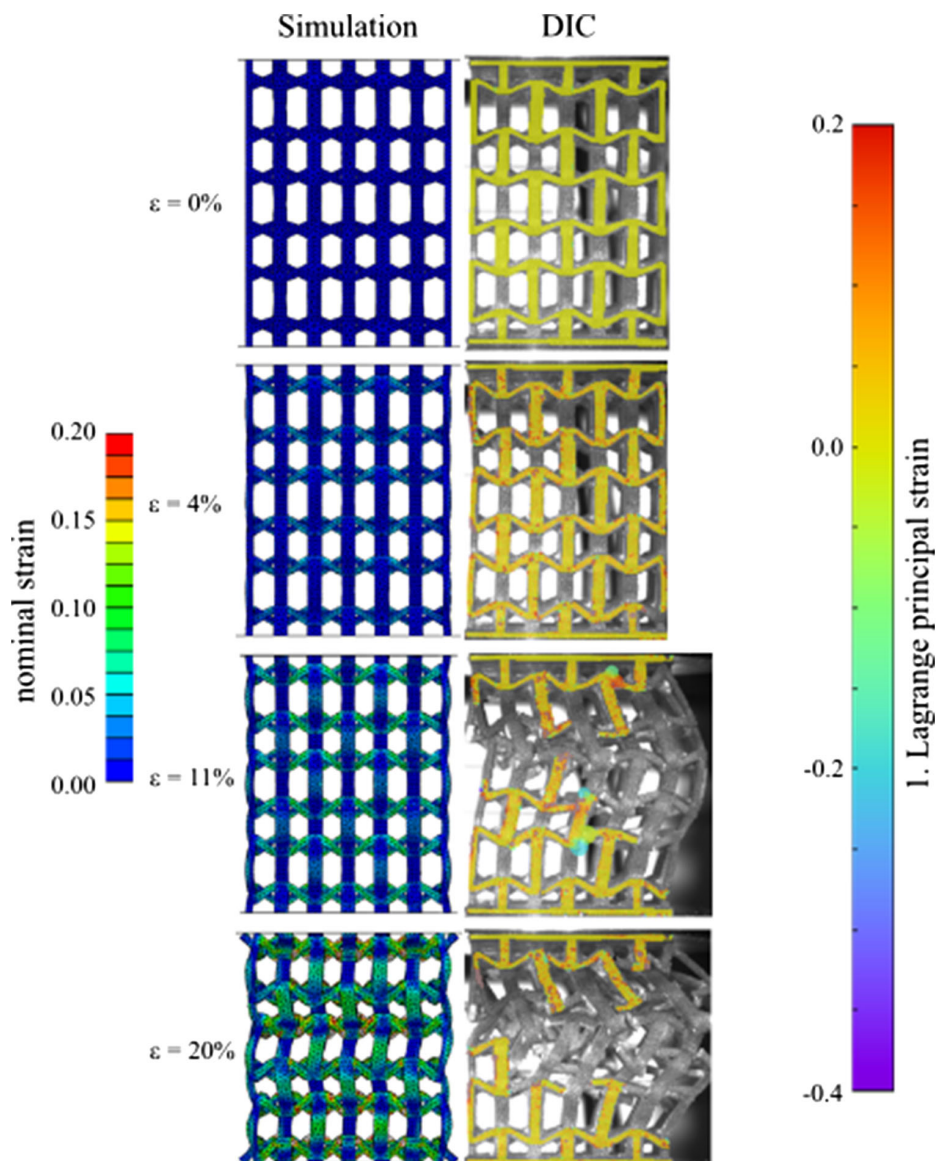

Figure 12. Comparison between simulation results (left) and DIC measurements (right) of a compression test for a S-3 uncoated specimen. The predicted deformation behavior differs from the experiment. The specimens shear out to one side, which is explained by inhomogeneities in the polyjet printed polymer.

ADVANCED
SCIENCE NEWS
www.advancedsciencenews.com

ADVANCED
ENGINEERING
MATERIALS
www.aem-journal.com

the optimization as only the geometry was optimized, and the same error in the model was made for each simulation.

The comparison of the stress–strain diagram for two configurations of S-4 (**Figure 13**a)) for the hollow strut specimens reveals that the optimized specimens (S-4B) are weaker in terms of PCS and plateau stress than the reference model S-4A. The reason is a folding of the hollow struts perpendicular to the loading direction for the bulbous S-4B specimens, which is revealed by a DIC analysis (**Figure 14**). Hence, the hollow strut S-4B specimens are rendered much weaker than predicted. The waisted struts of S-4A are just bending and thus are able to bear a higher compressive load. The specimens of S-4A are in addition able to absorb higher amounts of energy than the S-4B specimens (Table 3). Therefore, the hollow strut specimens of S-4A were used to compare with the other hollow strut specimens of S-3.

The hollow strut specimens of S-3 offer more than twice as high PCS and plateau stress compared with the S-4A specimens, as can be seen in the stress–strain diagrams of the hollow strut specimens (Figure 13b)). Furthermore, the application of twice the coating thickness increases the bearable stress nearly four times. This implies that the optimal coating thickness is above 120 μm.

The stress–strain behavior of the auxetic hollow strut structures with ≈5 pores per inch (ppi) compared with a conventional 20 ppi Ni/Al hybrid foam is shown in **Figure 15**. Both were coated with 120 μm nickel. The auxetic hollow strut structures endure up to two times higher PCS and plateau stresses. In addition, up to four times higher mass-specific stresses and thus a higher specific energy absorption capacity were reached, which shows the great lightweight potential of the auxetic structures.
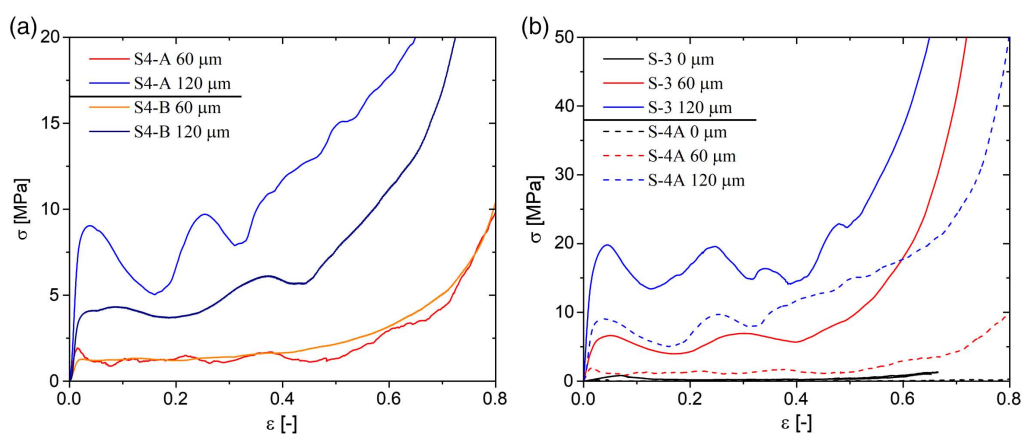

Figure 13. Stress–strain diagrams of a) the hollow strut structures for 60 μm nickel coating and 120 μm for both configurations of S-4; b) the hollow strut structures for 60 and 120 μm nickel coating, respectively, and the pure polymer specimens (0 μm) for S-3 and S-4A. The hollow strut specimens of the optimized S-4B fail early due to a folding of the struts, thus the S-4A specimens display a higher PCS and plateau stress and are used for comparisons. The hollow strut specimens of S-3 are superior to the S-4A specimens in terms of PCS and plateau stress and consequently have the higher energy absorption capacity.
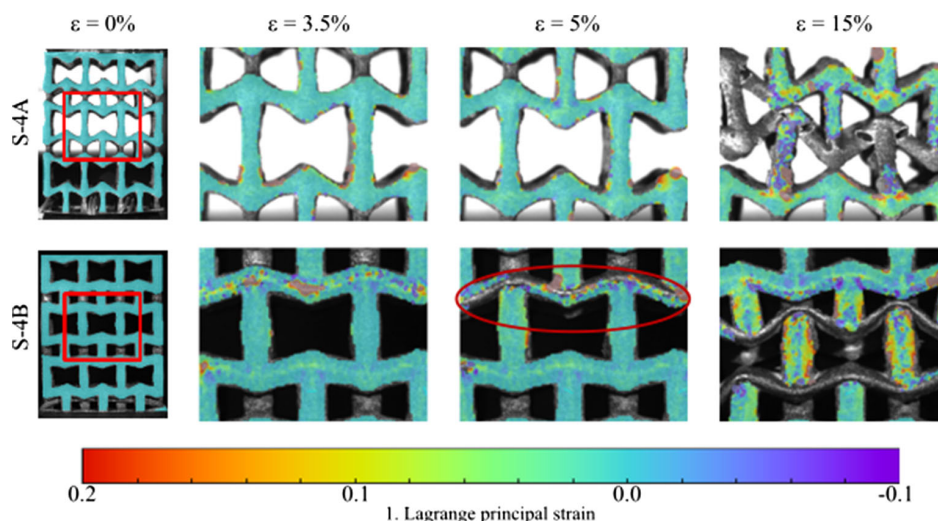

Figure 14. DIC comparison of both configurations of S-4 for different strain states. The region where the struts begin to fold for S-4B is marked with a red ellipse. The struts of S-4A only buckle under loading. A low signal-to-noise ratio in the DIC was obtained through the high resolution of the camera and the small speckle pattern.
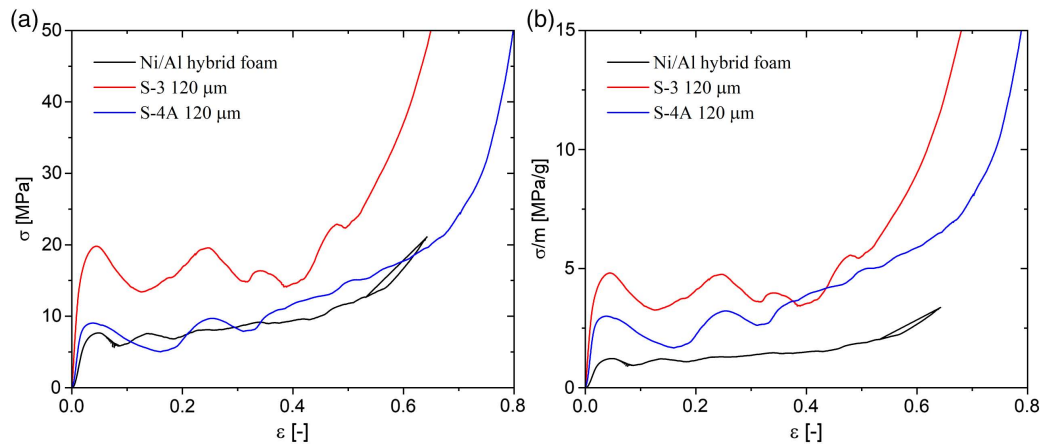
Figure 15. Comparison of the hollow strut structures of S-3 and S-4A with 120 μm thick nickel coating and a Ni/Al hybrid foam with 120 μm thick nickel coating a) stress–strain diagrams; b) mass-specific stress–strain diagrams. The hollow strut specimens outperform the Ni/Al hybrid foam especially in the mass-specific values.

The Poisson's ratio of the hollow strut structures were measured using DIC and compared with the predicted Poisson's ratio from the simulation. As the upper and lower struts were fixed on the plates only the middle layer of cells is crucial to the negative Poisson's ratio and thus only this part was measured as region of interest. To calculate the Poisson's ratio, the strain in loading direction and the strain in perpendicular direction from the region of interest were measured tracking the length of multiple lines over the course of the experiment (**Figure 16**).

Table 4 shows the measured Poisson's ratios for the different structures. All Poisson's ratios measured in the experiments were larger than expected from simulation. The reasons are, on the one hand, the hollow struts and, on the other hand, the different material. The simulation used the material parameters for the printer polymer and the hollow strut specimens were pure nickel. Furthermore, the hollow struts are more ductile and hence are able to undergo larger deformations. Therefore, the auxetic behavior is more visible compared with the brittle pure polymer specimens. For S-3, the Poisson's ratio differs only slightly for the two coating thicknesses. In the case of S-4A, the Poisson's ratio grows more negative with increasing coating thickness as the struts have higher bending stiffness, which leads to more plastic flow in the joints. The thicker nickel coating in the case of S-4B hinders the plastic deformation in the joints, as the vertical struts are already resistant to buckling on account of the belly.
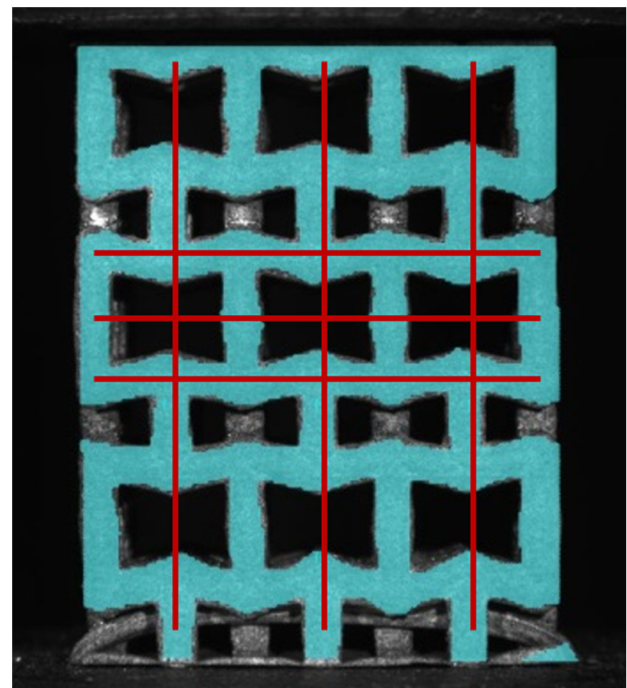
3.3. Dynamic Compression Experiment

The pure polymer specimens also show a brittle failure under dynamic loading. But they do not shear out like in the quasistatic case because there is not enough time for this deformation behavior as indicated by the images taken during the experiment (**Figure 17**). However, there is an increase in the stiffness under dynamic loading in the stress–strain diagram, but only in comparison with the quasistatic experiments (Figure 17). But as in the OHPB, there is a ramp-in effect,[58]

Figure 16. Poisson's ratio measurement scheme with DIC: the length of the red lines was tracked during the deformation and used to calculate the loading direction and perpendicular strains.

Table 4. Poisson's ratio for the different structures from the simulation and measured by DIC in the hollow strut compression experiments (exp.).

Specimen	ν Simulation	ν 60 μm exp.	ν 120 μm exp.
S-3	−0.12	−0.28	−0.31
S-4 A	−0.20	−0.24	−0.41
S-4B	−0.07	−0.38	−0.25

2001393 (11 of 15)

ADVANCED
SCIENCE NEWS
www.advancedsciencenews.com

ADVANCED
ENGINEERING
MATERIALS
www.aem-journal.com

the elastic part for low strains is problematic to evaluate, which means there is not necessarily a stiffness increase in the specimens. But the higher strain rate exhibits a plateau stress higher than in the quasistatic case, which occurs only for S-3. The S-4A pure polymer specimens were too weak to measure with the OHPB setup, and the S-4B pure polymer specimens do not exhibit any plateau stress but otherwise behave the same as the S-3 specimens.

The hollow strut structures with 60 and 120 μm nickel behave similarly under dynamic loading (**Figure 18**). There is no change in the stiffness from quasistatic to dynamic loading, although nickel should be strain rate dependent.[59] Only a small strain rate effect is visible in the PCS and the plateau stress. Both are larger for the high strain rate ($800 s^{-1}$) than for the low strain rate ($400 s^{-1}$) and the quasistatic experiments.

The optimized S-4B specimens exhibit the same failure mechanism as in the quasistatic experiments. Therefore, there is no difference between the results of the S-4A and the S-4B

specimens concerning the stress–strain behavior. The S-3 specimens exhibit an increase in the PCS and the plateau stress by approximately three times compared with both S-4 specimens. The 120 μm nickel coating triples the PCS and plateau stress for all specimens in comparison with the 60 μm nickel specimens.

The measured strain rates deviate from the desired strain rates (**Figure 19**) due to inhomogeneities in the specimens concerning their coating thickness. But within a small margin of error, the desired strain rates were well matched. Also in terms of comparability, almost all strain rates are larger than expected. The curves in Figure 19 are mean values over all experiments with the standard deviation shown in **Table 5**. The pure polymer specimens scatter the least, with the exception of the S-4A pure polymer specimens. The most homogeneous coated specimens were the S-4B hollow strut specimens. The measured strain rates scatter a lot for the 120 μm nickel S-3 hollow strut specimens (Table 5) due to inhomogeneities in the coating.
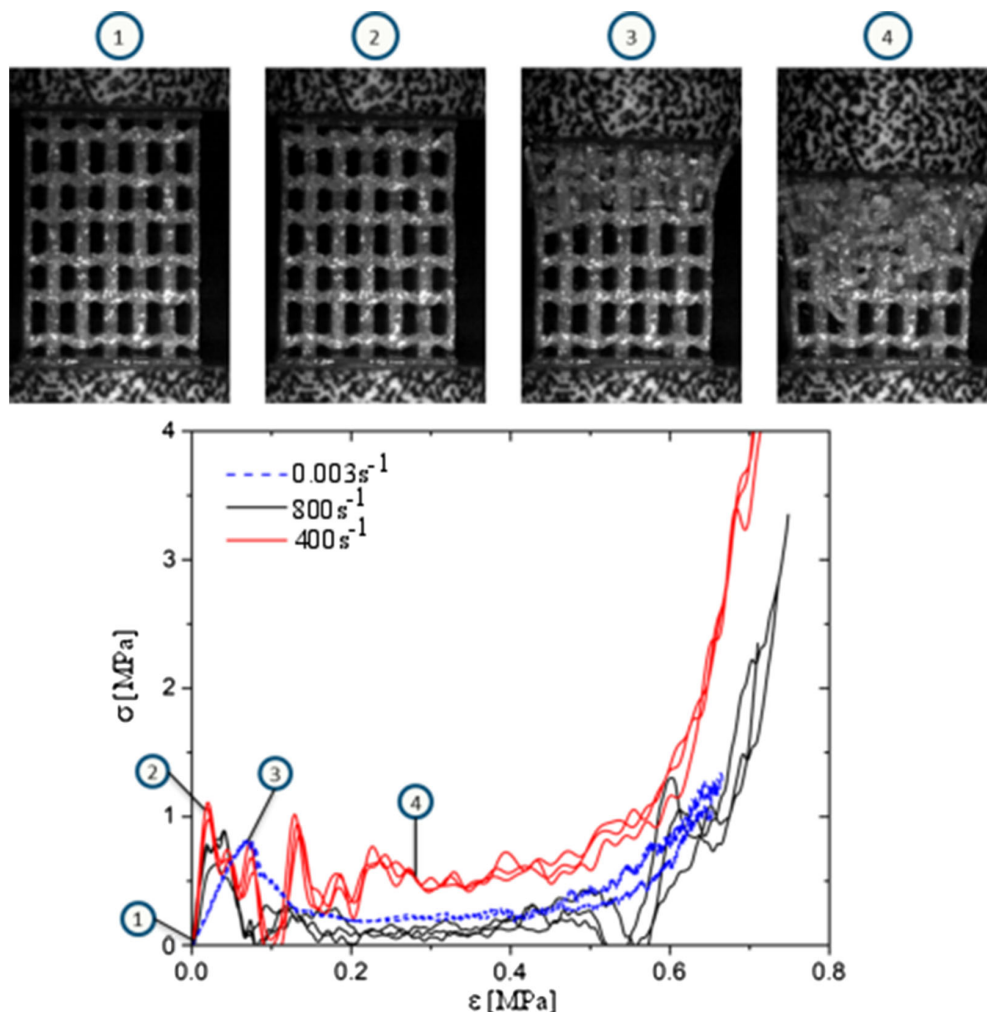

Figure 17. Images taken at specific strains to demonstrate the local failure mechanism (upper row). Stress–strain diagrams of OHPB and quasistatic results for S-3 pure polymer specimens (lower row), $0.003 s^{-1}$ belongs to the quasistatic strain rate. The specimens are crushed and have not enough time to shear out as they did in the quasistatic experiments. The PCS and plateau stress are slightly increased under dynamic loading.
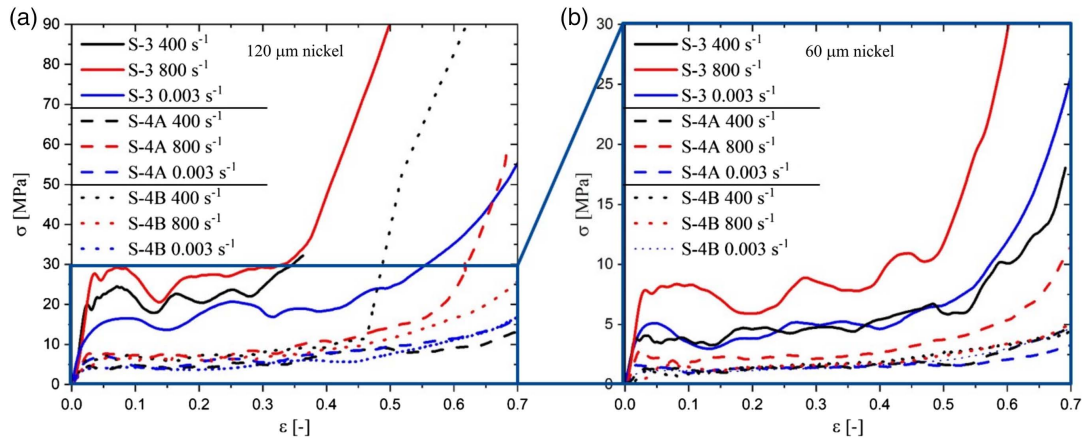
Figure 18. Mean stress–strain diagrams of the hollow strut structures; 400 and 800 s^{-1} are the dynamic strain rates and 0.003 s^{-1} is the quasistatic strain rate; a) 120 μm nickel and b) 60 μm nickel. The PCS and plateau stress are increased under dynamic loading and twice the coating thickness enhances the endured stress approximately by a factor of three. The specimens of S-3 show the highest PCS and plateau stress.
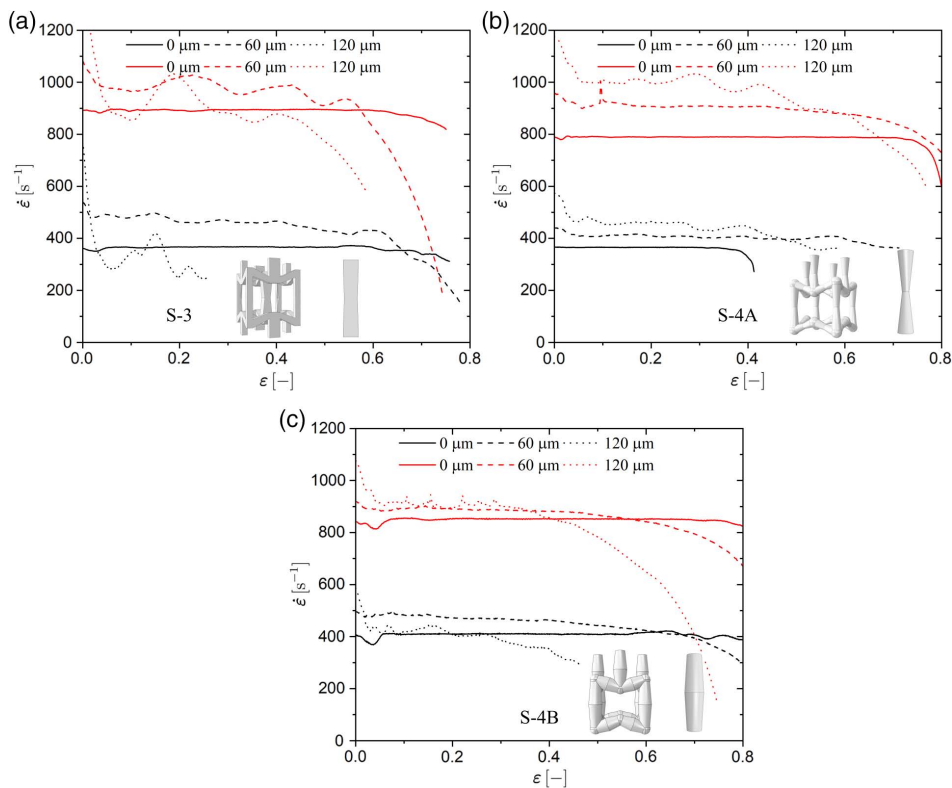

Figure 19. Mean measured strain rates of the OHPB experiments for the pure polymer specimens ($_0$ μm) and the two nickel coating thicknesses of hollow strut specimens (60 and 120 μm) of the three different structures: a) S-3, b) S-4A, and c) S-4B. The lower strain rate is marked in black and the higher strain rate in red. The corresponding unit cell and a representative strut are depicted in each diagram. There is a small deviation from the desired strain rates to higher ones as a result of inhomogeneities.

4. Conclusion

The present contribution showed that it is possible to use finite element simulations to enhance cellular auxetic materials significantly using just two geometry parameters. Hence, a tailoring of the material for specific needs such as the specific energy

absorption capacity is easily possible. The simulations were well matched by the experiment in the elastic region of the stress–strain diagram, but not for the plastic part. Consequently, the simulations overestimated the energy absorption capacity for all simulated models. This is caused by too few material parameters provided by the manufacturer, a more brittle behavior than

**ADVANCED
SCIENCE NEWS**

www.advancedsciencenews.com

**ADVANCED
ENGINEERING
MATERIALS**

www.aem-journal.com

Table 5. Standard deviation $\tilde{S}$ of the mean strain rate for all dynamic experiments, 0 μm belongs to the pure polymer specimens, 60 and 120 μm are the corresponding hollow strut specimens.

$\tilde{S}$ [s^{-1}]	S-3		S-4A		S-4B	
	400 s^{-1}	800 s^{-1}	400 s^{-1}	800 s^{-1}	400 s^{-1}	800 s^{-1}
0 μm	12.76	25.85	92.05	14.10	20.17	26.89
60 μm	100.61	54.48	77.15	78.44	17.39	19.34
120 μm	80.86	88.85	26.67	28.70	48.05	31.47

expected and a disregard of damage in the simulations. Nevertheless, the simulations provide valuable insights for the structural optimization but cannot replace an experimental investigation. Thin struts lead to relatively high Poisson's ratios but poor energy absorption capacity, whereas thick struts will increase the energy absorption capacity but lower the auxetic effect. In the future, the simulations can be improved by micromechanical experiments and consideration of cracks.

The combination of AM and electrochemical coating enables an improvement of cellular lightweight materials, as outlined in this work. A subsequent heat treatment of the coated specimens to melt out the polymer is mandatory to achieve a ductile failure behavior. Thereby, the energy absorption capacity is strongly enhanced and the effect of the negative Poisson's ratio is better observable even for larger strains. The quasistatic and dynamic experiments proved the high energy absorption capacities, especially compared with common 20 ppi Ni/Al hybrid foams. Furthermore, the nickel hollow strut specimens increased their energy absorption capacity for higher strain rates, which makes them even more suitable for applications as crash absorbers in cars or trains. As the designer does not have to consider a change in the stiffness for higher deformation rates, auxetic cellular materials are highly recommended for applications in automotive industry. The specimens in this contribution all displayed a negative Poisson's ratio, which was more negative than expected from the simulations. The DIC further revealed a different deformation behavior for the pure polymer specimens for the quasistatic experiments than predicted by the simulations. Due to material inhomogeneities, the specimens shear our in one direction. The DIC also discloses the reason for the early failure of the optimized S-4B specimens. The bulbous struts are folding, resulting in a failure of the coating rather than a failure of the structure.

In summary, the possibility of AM enables the fabrication of tailored metamaterials for crash absorbers and further enhancement of such materials through electrochemical coating can be achieved. These tailored cellular materials are worth further investigation to provide more safety in case of accidents in transportation industry.

Acknowledgements

Conflict of Interest

The authors declare no conflict of interest.

Data Availability Statement

Research data are not shared.

Keywords

[1] R. Lakes, *Nature* **1992**, *358*, 713.
[2] A. Alderson, K. Alderson, *J. Aerospace Eng.* **2007**, *221*, 565.
[3] T.-C. Lim, *Mech. Adv. Mater. Struct.* **2015**, *22*, 205.
[4] K. L. Alderson, V. R. Simkins, V. L. Coenen, P. J. Davies, A. Alderson, K. E. Evans, *Phys. Status Solidi B* **2009**, *242*, 509.
[5] R. Lakes, *Science* **1987**, *235* 1038.
[6] R. Lakes, K. Elms, *J. Compos. Mater.* **1993**, *27*, 1193.
[7] M. Bianchi, F. Scarpa, C. Smith, *Acta Mater.* **2010**, *58*, 858.
[8] R. Lakes, *J. Mech. Design* **1993**, *115*, 696.
[9] A. Bezazi, F. Scarpa, *Int. J. Fatigue* **2007**, *29*, 922.
[10] F. Scarpa, P. Pastorino, A. Garelli, S. Patsias, M. Ruzzene, *Phys. Status Solidi* **2005**, *242*, 681.
[11] N. Novak, M. Vesenjak, Z. Ren, *Sci. Technol. Mater.* **2018**, *30*, 4.
[12] N. Novak, L. Starčevič, M. Vesenjak, Z. Ren, *Composite Structures* **2019**, *210* 167.
[13] J. Choi, R. Lakes, *Cell. Polym.* **1991**, *10*, 205.
[14] B. Caddock, K. Evans, *Biomaterials* **1995**, *16*, 1109.
[15] R. Almgren, *J. Elast.* **1985**, *15* 427.
[16] J. N. Grima, K. E. Evans, *J. Mater. Sci. Lett.* **2000**, *19*, 1563.
[17] A. Yeganeh-Haeri, D. J. Weidner, J. B. Parise, *Science* **1992**, *257*, 650.
[18] V. Gorodtsov, D. Lisovenko, *Mech. Solids* **2020**, *55*, 461.
[19] W. Wu, D. Qi, H. Liao, G. Qian, L. Geng, Y. Niu, J. Liang, *Sci. Rep.* **2018**, *8*, 1.
[20] Z. Lu, Q. Wang, X. Li, Z. Yang, *Int. J. Solids Struct.* **2017**, *124* 46.
[21] H. Yang, B. Wang, L. Ma, *Int. J. Solids Struct.* **2019**, *180* 13.
[22] T. Fíla, P. Zlámal, O. Jiroušek, J. Falta, P. Koudelka, D. Kytyř, T. Doktor, J. Valach, *Adv. Eng. Mater.* **2017**, *19*, 1700076.
[23] A. Mauko, T. Fíla, J. Falta, P. Koudelka, V. Rada, M. Neuhäuserová, P. Zlámal, M. Vesenjak, O. Jiroušek, Z. Ren, *Metals* **2021**, *11*, 52.
[24] N. Novak, M. Vesenjak, S. Tanaka, K. Hokamoto, Z. Ren, *Int. J. Impact Eng.* **2020**, 103566.
[25] K. E. Evans, M. Nkansah, I. Hutchinson, S. Rogers, *Nature* **1991**, *353*, 124.
[26] C. He, P. Liu, A. C. Griffin, *Macromolecules* **1998**, *31*, 3145.
[27] J. Clarke, R. Duckett, P. Hine, I. Hutchinson, I. Ward, *Composites* **1994**, *25*, 863.
[28] C. T. Herakovich, *J. Compos. Mater.* **1984**, *18*, 447.
[29] A. Alderson, J. Rasburn, K. E. Evans, *Phys. Status Solidi B* **2005**, *244*, 817.
[30] K. Alderson, A. Alderson, G. Smart, V. Simkins, P. Davies, *Plast. Rubber Compos.* **2002**, *31*, 344.
[31] T. A. Schaedler, W. B. Carter, *Annu. Rev. Mater. Res.* **2016**, *46*, 187.
[32] O. Querin, G. Steven, Y. Xie, *Eng. Comput.* **1998**, *15*, 1031.
[33] G. I. Rozvany, M. Zhou, T. Birker, *Struct. Optim.* **1992**, *4*, 250.

**ADVANCED
SCIENCE NEWS**

www.advancedsciencenews.com

**ADVANCED
ENGINEERING
MATERIALS**

www.aem-journal.com

[34] C. G. Broyden, *IMA j. Appl. Math.* **1970**, *6*, 222.

[35] R. Fletcher, *Comput. J.* **1970**, *13*, 317.

[36] D. Goldfarb, *Math. Comput.* **1970**, *24*, 23.

[37] D. F. Shanno, *Math. Comput.* **1970**, *24*, 647.

[38] J. Nocedal, S. J. Wright, *Numerical Optimization*, 2nd ed, Springer, New York **2006**.

[39] R. Byrd, P. Lu, J. Nocedal, C. Zhu, *SIAM J. Sci. Comput.* **1995**, *16*, 1190.

[40] A. Standard, P. Jain, AM Kuthe, *Proc. Eng.* **2013**, *63* 4.

[41] X. Wang, M. Jiang, Z. Zhou, J. Gou, D. Hui, *Compos. Part B: Eng.* **2017**, *110* 442.

[42] B. Tymrak, M. Kreiger, J. Pearce, *Mater. Design* **2014**, *58* 242.

[43] B. Caulfield, P. McHugh, S. Lohfeld, *J. Mater. Process. Technol.* **2007**, *182*, 477.

[44] H. Gu, C. Ma, J. Gu, J. Guo, X. Yan, J. Huang, Q. Zhang, Z. Guo, *J. Mater. Chem. C* **2016**, *4* 5890.

[45] R. Singh, V. Singh, M. S. Saini, in *ASME 2010 International Mechanical Engineering Congress And Exposition*, American Society of Mechanical Engineers, New York, NY *2010* pp. 1049–1053.

[46] R. Singh, *Adv. Mater. Res.* **2010**, *83*, 342.

[47] K. V. Wong, A. Hernandez, *ISRN Mech. Eng.* **2012**, *2012*, 1.

[48] P. Koudelka, M. Neuhauserova, T. Fíla, D. Kytyř, *Appl. Mech. Mater.* **2016**, *821* 428.

[49] K. Wang, Y.-H. Chang, Y. Chen, C. Zhang, B. Wang, *Mater. Design* **2015**, *67* 159.

[50] X.-T. Wang, X.-W. Li, L. Ma, *Mater. Design* **2016**, *99* 467.

[51] A. Jung, S. Diebels, *Adv. Eng. Mater.* **2016**, *18*, 532.

[52] A. Jung, H. Natter, R. Hempelmann, S. Diebels, M. R. Koblischka, U. Hartmann, E. Lach, *ECS Trans.* **2010**, *25*, 165.

[53] A. Jung, H. Natter, S. Diebels, E. Lach, R. Hempelmann, *Adv. Eng. Mater.* **2011**, *13*, 23.

[54] A. Jung, M. R. Koblischka, E. Lach, S. Diebels, H. Natter, *Int. J. Mater. Sci.* **2012**, *2*, 97.

[55] A. Jung, J. Wocker, Z. Chen, H. Seibert, *Mater. Design* **2015**, *88* 1021.

[56] R. A. Govender, R. J. Curry, *J. Dyn. Behav. Mater.* **2016**, *2*, 43.

[57] T. Fíla, P. Koudelka, J. Falta, P. Zlámal, V. Rada, M. Adorna, S. Bronder, O. Jiroušek, *Int. J. Impact Eng.* **2020**, 103767.

[58] T. Fíla, P. Koudelka, P. Zlámal, J. Falta, M. Adorna, M. Neuhäuserová, J. Luksch, O. Jiroušek, *Adv. Eng. Mater.* **2019**, *21*, 1900204.

[59] A. Jung, A. Pullen, W. Proud, *Compos. Part A: Appl. Sci. Manufact.* **2016**, *85* 1.

2001393 (15 of 15)